

Unified description over time of heterogeneous condensation with quenched disorderRuddy Urbina * and Wenceslao González-Viñas †*Universidad de Navarra, Department of Physics and Applied Mathematics, E-31008 Pamplona, Spain* (Received 5 October 2022; revised 1 December 2023; accepted 4 December 2023; published 27 December 2023)

We report experimental results on breath figures (BFs) observed on substrates with quenched disorder. The evolution of BFs is found to be primarily influenced by global parameters associated with boundary conditions. We investigate classical statistical measures and explore topological properties using persistent homology techniques based on a modified Vietoris-Rips complex. Our findings reveal that the evolution of the number surface density of condensed droplets plays a crucial role in determining various condensation stages previously considered distinct. This evolution is significantly influenced by the distribution of nucleation sites and the individual growth law governing water droplets when coalescence does not occur. Ultimately, we demonstrate the capability to predict coalescence events based on the topological characteristics of BFs at a given point in time.

DOI: [10.1103/PhysRevE.108.065107](https://doi.org/10.1103/PhysRevE.108.065107)**I. INTRODUCTION**

The evolution of systems with quenched disorder has been regarded as difficult to deal with. Usually, the approach is bottom-up, where the Hamiltonian of the isolated elements is known, as well as the interaction among them. *A posteriori* the quenched disorder is set up, and to solve the dynamics one has to rely upon now well-established techniques (replica trick, cavity method, among others) [1]. However, a holistic approach has not been considered so far due to the limited information it is believed to be able to retrieve.

Our model system consists of dropwise heterogeneous condensation on a surface, which is a first-order out-of-equilibrium phase transition. Breath figures (BFs) are two-dimensional (2D) patterns consisting of those condensed droplets. The surface is in a condition of supersaturation for a vapor (in our work, water vapor), while the surrounding atmosphere is not. BFs begin by the nucleation of tiny droplets, generally in places where the energy barrier for nucleation has been lowered (by imperfections, impurities, etc.), and evolves by the growth of the droplets by direct condensation and coalescence [2,3]. BFs have been used extensively in the past to recover water from atmospheric humidity for irrigation and drinking water [2]. Also, heterogeneous condensation has been proven an efficient method to increase heat transfer [3] because the latent heat is transferred to the substrate directly.

In this article we address two intertwined objectives. First, to find a unified description for different regimes of the BF dynamics, seemingly unconnected with each other, by using the spatial distribution of nucleation sites. This would shed light on the quenched disorder occurring naturally on surfaces where dropwise heterogeneous condensation takes place and its effects on the BF. We bring evidence of the connection

between the global characteristics of the boundary conditions and the observed dynamics. Second, to associate certain static (spatial) topological properties with the dynamics of the system. Our approach involves a modified concept that naturally emphasizes the distance between droplet surfaces as a significant factor, in contrast to other conventional measures that overlook this aspect.

BF dynamics is mainly determined by the environmental conditions and surface properties such as wettability, roughness, and heterogeneity, which play a key role in this matter. Previous works (see for a review [3]) have shown that those properties may alter the nucleation rate, which in turn affects the timescales of the BF dynamics, the maximum value of surface coverage, and the droplet size distribution. The most common properties described in the literature include the surface coverage ε^2 (ratio of substrate's area covered by the droplets to the total area), the droplet number density, and the average radius as they evolve in time, to compare the performance of surfaces and/or environmental conditions. Spatial heterogeneity in the surfaces has been explored concerning the dimensionality of the substrate, its finite size [4], wettability [5], hygroscopicity [6,7], drop shedding [8,9], and contact angle pinning and hysteresis [10]. Almost all the studies have considered ordered arrays of loci (e.g., [5,7]). However, the most common everyday-life heterogeneity is genuinely disordered, and related to impurities and imperfections which are intrinsic to the surfaces, or appeared later (e.g., dust particles).

The evolution of BFs usually displays up to six stages [2] to which we will refer through this article: (1) Initial nucleation. (2) Isolated growth by water vapor absorption, where almost all the droplets are separated at a distance much larger than their radii, hindering their interaction. Here the radius of each droplet grows as $t^{1/2}$ [11]. (3) As droplets continue their growth, the interdroplet distance gets smaller, allowing neighboring droplets to interact through the atmosphere. Absorption is diminished because of the overlapping of concentration profiles around single droplets, and the average

*rurbina@alumni.unav.es

†wens@unav.es

radius becomes $\propto t^{1/3}$. (4) Growth by coalescence and water molecules absorption, where coalescence events become more frequent and their contribution to the growth now dominates over the absorption, leading to an average radius growth $\sim t^1$. Additionally, the surface coverage (proportion of the surface covered by droplets) reaches a constant value, which means that the droplet separation scales with the average radius of the droplets. (5) Nucleation of new droplets. When two or more droplets coalesce, they sweep a section of the substrate where nucleation may start over again. If the section is large enough, the growth of the new droplets follows the same growth behavior described earlier. (6) Finally, gravity effects become relevant leading to drop deformation and/or shedding. These regimes usually overlap or even are not present in a given system depending on the experiment conditions [3]. For example, droplets in stages 2 and 3 may undergo a significant number of coalescence events, as is observed usually when the number of droplets is plotted against time. We show that this complexity can be simplified by unifying stages 2–4.

In general, the microscopic mechanisms behind the evolution of BFs are still not well known [12] and may vary depending on the experimental conditions. Currently, most of the models are focused on some of the aforementioned stages and in some aspects, as happens with the number density of droplets [13–16] or the distribution of droplet sizes [17]. The main models describing this fact come from the scaling of the cluster size distribution in aggregation processes [18].

The nucleation of water droplets on substrates occurs as a thermally activated process. On a perfectly homogeneous surface, the nuclei appear randomly and progressively, and quenched disorder is not present. However, the energy barrier to forming viable (i.e., thermodynamically stable) water droplets can be lowered through impurities or imperfections. Their location may be either tailored (e.g., in the form of lattices) or statistically random like in natural environments.

The present work considers substrates with quenched disorder induced by a coating on a glass surface. By quenched disorder, we refer to a static, disordered distribution of nucleation sites on the substrate. These nucleation sites do not relax at the relevant times of the experiment. We ensure the quenched disorder by also conducting the experiments at supersaturation level lower than the critical level for condensation in places outside the nucleation sites. While a few studies have focused on disorder, they had different objectives and approaches than ours. In one study [19], the authors reported experimental results of condensation on substrates coated similarly to ours, but their focus was mainly on the coalescence-dominated regime, and they did not vary the density of nucleation sites. In another study [9], the authors focused on water collection using different roughness substrates obtained by sandblasting, which increased the number of nucleation sites without significantly changing the macroscopic contact angles. As a result, coalescence events were more frequent, and the volume of collected water increased.

It is known that relevant mesoscopic information about systems can be obtained by using persistent homology (PH) techniques [20], which highlight topological structures that persist across a range of spatial scales. These methods have been previously used to explore the degree of compaction in granular systems [21] and to identify structural features

in colloids that cannot be distinguished using classical techniques [22], among many other applications. To use PH tools, a set of objects and a filtration parameter must be defined to construct a filtration of simplicial complexes that represent the configurational states (see Sec. III).

In this article we investigate the evolution of dropwise condensation patterns on surfaces with quench disorder and different densities of randomly distributed nucleation sites while keeping all other experimental conditions constant. In Sec. II we describe the experimental setup and procedures. In Sec. III we introduce the persistent homology techniques. In the following sections, we present the results, discussion, and conclusions of the study.

II. EXPERIMENTS

To experimentally study the evolution of BFs, we use a condensation chamber consisting of a cylindrical polymethyl methacrylate container that encloses a Peltier device where the substrate is placed. The Peltier rests on a copper heat exchanger with water recirculation coming from a refrigerated water bath. The chamber is connected with two opposed air entrances that inject humid filtered air (with a relative humidity of about 70% at 21 °C, corresponding to $T_{\text{dew}} = 15.3$ °C). The conditions are set to promote heterogeneous condensation on the substrate. The air is streamed at a constant total flow rate of 140 ml/min, while the temperature is controlled by the Peltier device that keeps the substrate at a constant temperature $T_s = 10$ °C (for which the humidity level is supersaturated at a 1.42 value, smaller than the value to have condensation on the measured macroscopic contact angles; see [3] and Supplemental Material [23]). The BF is observed through an optical window with a reflection optical microscope attached to a complementary metal oxide semiconductor (CMOS) camera. A region of interest in the center of the substrate is focused.

The substrates are glass slides, either bare or coated, of 25 mm \times 30 mm which are cleaned, coated (if it applies), and characterized individually for each experiment. The cleaning procedure consists of the following steps: the substrates are rinsed with acetone, ethanol, and ultra-pure water. Next, an RCA SC-1 cleaning process is undertaken: they are immersed in a basic piranha (5:3:1 ultra-pure water, H_2O_2 33%, and ammonia 25%) for 40 min at 60 °C. Then the substrates are rinsed with ultra-pure water and immersed in ultra-pure water for 5 h before the coating process, for which we used a solution of OTS (octadecyltrichlorosilane) in HMDSO (hexamethyldisiloxane) which leaves on the surface some impurities that promote nucleation [19]. Their number density depends on the concentration and the time the surface is submerged into the solution. We employed concentrations between 5% (v/v) and 10% (v/v) of OTS in HMDSO and waited for time intervals of 5–10 min. The coating solution is prepared and vigorously stirred before carefully placing the dry slide inside. The substrate is then extracted from the solution, excess liquid is removed, and the glass is dried in a stove at 60 °C for 30 min. The substrate is later stored in a clean container for 24 h. Finally, on the usable coated substrates we measured the macroscopic contact angles θ_a and θ_r of the surface with ultra-pure water. These values, the coating time, and concentration c for all the samples are shown in Table 1 of the

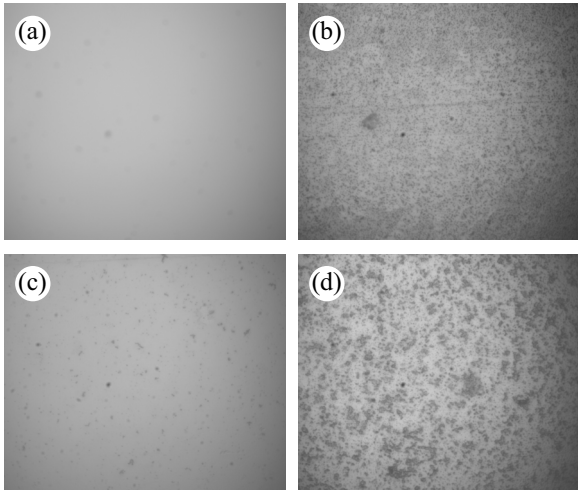


FIG. 1. Substrates before the experiment. (a) Bare substrate (none) and coated substrates with (b) low, (c) intermediate, and (d) high nucleation site densities. HFOV (horizontal field of view): (a) 1.104 mm and (b)–(d) 0.220 mm. Dark spots and clusters are visible in [(b)–(d)], while optical artifacts from the objectives and the microscope can be observed in all the images and are removed in the analysis. Generally, these artifacts are present in all the images observed at the same magnification (regardless of the substrate), and they appear unfocused.

Supplemental Material [23]. All the substrates referred to in this study were used once, even though there is no appreciable aging on the coating after one experiment over the range of several days. We compare the results from the bare substrate with those from various coating densities, quantified by their initial number surface density ρ_0 of nuclei. From now on, the number surface density will be called density.

The contact angles mainly affect the volume coefficient of a droplet γ . This coefficient is defined as the ratio of the droplet volume to its apparent radius cubed. The apparent radius is the radius of the projected droplet onto the substrate. In the case of a spherical cap-shaped droplet, γ depends on the contact angle θ . If the droplet is perfectly hemispherical, $\gamma = 2\pi/3$. If $180^\circ \geq \theta \geq 90^\circ$: $\gamma = \frac{\pi}{3}(2 - 3\cos\theta + \cos^3\theta)$ [2], and if $0^\circ < \theta \leq 90^\circ$: $\gamma = \frac{\pi(1-\cos\theta)(2+\cos\theta)}{3(1+\cos\theta)\sin\theta}$.

It is worth noting that, when the coalescence events are statistically not dominant, droplet growth is mostly dominated by moisture absorption, so $\theta = \theta_a$ and γ are essentially constant in each experiment. When two droplets coalesce, the contact line in the farthest points recedes, and in the contact point, advances. Thus, in the times when there is a significant increment of coalescence events, the receding angle plays an important role and, in consequence, θ varies between (θ_r, θ_a) even for a specific droplet at a given time. Then γ may change along time, but the contact angle may be approximated as the mean angle $\theta_m = (\theta_a + \theta_r)/2$ [9]. The experiment on an uncoated substrate (named “none”) shows stronger deviations, associated with a lower receding contact angle and relatively high contact angle hysteresis, implying that the assumption of a spherical cap may not be applicable throughout the experiment [10].

Before the experiment begins, an initial micrograph of the substrate is taken. Figure 1 shows these images for each of the

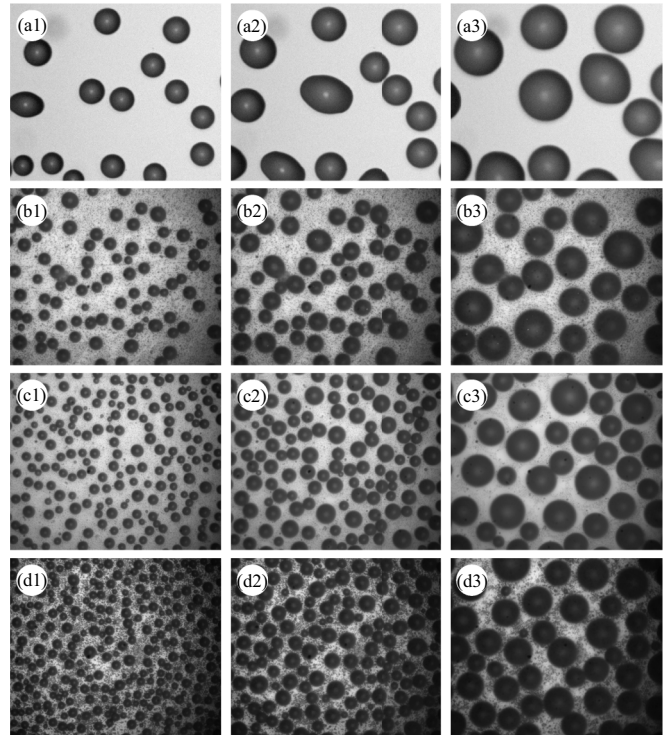


FIG. 2. Snapshots of the BF evolution for all substrates: (a) none, (b) low, (c) intermediate, and (d) high, at three different times: 1, 180 s; 2, 402 s; and 3, 900 s (a3, 901 s). All the condensation patterns were obtained under the same experimental conditions. HFOV is 0.22 mm (for panel a, cropped to 0.22 mm).

cases: three coated samples labeled according to the density of active nucleation points (low, intermediate, and high) and an uncoated sample (none) for comparison. Right after, the inflow of humid air is activated and the Peltier is switched on. This time is set as the origin ($t = 0$) of the experiment, and snapshots of the evolving breath figures on the substrates are taken regularly. The experimental conditions in the condensation chamber are observed to be stationary about 3 min after the beginning of the experiment. Thus, in this work we focus on the dynamics occurring between this point ($t = 3$ min) and around 40 to 60 min (depending on the substrate), while also avoiding the intense regime of nucleation at very short times. The latter will be considered in future works.

Figure 2 shows the droplet pattern at 180, 402, and 900 s for each of the four substrates. Within the same time interval, it is observed that the droplets grow faster on substrates with lower density. As known [12], $V \sim \sqrt{F}\Delta p$, where V is a droplet condensed volume, F is the air flux, and Δp is the difference between the partial water vapor pressure of the air and the saturation pressure at the substrate temperature. It is worth noting that all our experiments had the same values of air flux and saturation, leading to the same constant rate of increase of the total condensed volume per unit area, h , in the stationary state, for all substrates.

Many of the imperfections or impurities on the substrate may act as nucleation sites, although with our experimental setup, we are not able to determine whether all of them do so or not. We observe that imperfections may give rise to

tiny droplets at any time, although most of the nucleation events occur in the first 3 min of the experiment (which are not considered in this work) or at long times when new droplets appear [3]. The reduction of the energy barrier in each imperfection is distinct due to geometrical or composition factors, and some of those imperfections may remain dormant throughout the experiment, because of neighboring imperfections that act as humidity sinks, thus favoring condensation on themselves [24], rather than in the surroundings. Moreover, on some nucleation sites, water droplets grow and eventually stop growing while they are small, and they do not become part of the “main” breath figures’ evolution for the rest of the experiment [compare the backgrounds of Fig. 2(c1) to Fig. 2(c3) with Fig. 1(c)]. We do not consider these droplets since they do not appreciably evolve during the BF dynamics. This is also due to the (modified) local humidity profile [25] around them. In less common cases, some water droplets grow and, after some time, evaporate. Thus, there is a complex interaction between the sites themselves, the breath figure, and the environment. This is statistically relevant at short times when even growing droplets remain small. However, we do not take this regime into account because we focus on the experiment at times greater than 3 min after starting it, as already mentioned.

Snapshot image processing is implemented in Python routines to detect the droplets in the images. In each snapshot the centers and radii (of the projection on the substrate) of all the drops are estimated. In cases where the droplets were elongated (which occurred especially after coalescence in the none case, because the receding contact angle in this surface was low), it was used an equivalent radius \sqrt{ab} , where a and b are the semiaxes of the fitting ellipse. Based on this geometrical information, macroscopic quantities can be calculated such as the droplet number surface density ρ (number of droplets to the total surface area), the average droplet radius (r), and the droplet surface coverage ε^2 . These variables are commonly used to characterize the BF evolution. We also obtain information about mesoscales related to the randomness, structure, and topology of the system. The code being used is homemade and is based on several open-source libraries.

Further details of the experimental setup, procedure, and analysis of results are given in the Supplemental Material [23] and in previous works by the authors (e.g., [19]).

III. PERSISTENT HOMOLOGY

The droplets from a BF on a substrate at a given time can be considered as the nodes of a simple graph, where two droplets are linked if their interdistance is smaller than or equal to a given value, named the filtration parameter δ . In such a planar graph, we can identify n -dimensional simplices (where n goes from 0 to 2, corresponding to points, line segments, and triangles). If the induced subgraph by (any) three given nodes is complete, then a 2D simplex is defined for them. In that case, the graph would correspond to a simplicial complex K , called the Vietoris-Rips complex (VRC). A simplicial complex (or simply, complex) is a set of simplices with the following properties: every face of a simplex of the complex is in the complex, and the nonempty intersection of two simplices in

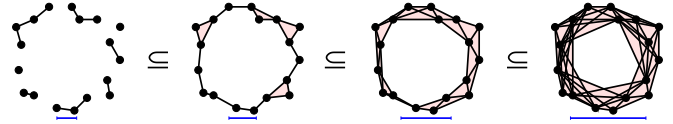


FIG. 3. Invented filtration to illustrate that a relevant hole persists in a long range of filtration parameters. The filtration parameter δ is depicted in blue and is the threshold distance that allows the creation of links (and triangles) in the complex.

the complex is a face of both. These complexes can be generalized to abstract spaces where the points or nodes are not necessarily defined in \mathbb{R}^n , and the filtration parameter is not compared to a distance to define the links of the complex.

A BF at a certain time, with a given filtration parameter, is, thus, a simplicial complex. A filtration is an ordered sequence of simplicial complexes with the inclusion relation. With the previous definitions, if $\delta_a \leq \delta_b \Rightarrow K(\delta_a) \subseteq K(\delta_b)$. Also in a complex, it is possible to define the group of chains at each dimension s that corresponds to any linear combination of s -dimension simplices (here with coefficients in \mathbb{Z}_2), the group of cycles (chains with null boundary), and the group of boundaries (cycles that are boundaries of a chain). The quotient group of the set of cycles with the set of boundaries is called the homology group H_s of the simplicial complex at a given dimension s . In this framework, the basis of the homology group corresponds to the different linearly independent holes (i.e., cycles that are not boundaries). The dimension of such a group is called the Betti number β_s of the complex at the given dimension s . Thus, β_0 is the number of connected components of the complex and β_1 is the number of independent holes (cycles of the VRC that are not triangles).

When a filtration is defined, we can characterize the persistence of the homology, i.e., the “length” in the filtration parameter space of the aforementioned topological features. Formally, for all dimension s , $K(\delta_a) \subseteq K(\delta_b)$ induces a linear map $H_s[K(\delta_a)] \mapsto H_s[K(\delta_b)]$. In this way, we can identify each feature along the filtration and set its birth filtration parameter value, in addition to its death value, which allows us to build the persistence diagram and the barcode (among other representations), where the latter represents the intervals at which all features live. The longest living features are the most relevant in the corresponding filtration (Fig. 3).

In the systems mentioned above [21,22], the nodes (particles) are finite spheres, monodisperse in size, that provide a characteristic length of the system which leads to a minimum filtration parameter to connect the particles in the graph. Also, note that their particle size is constant in time. This length allows us to obtain dimensionless quantities, in such a way that the system is comparable at different times.

In our system we are interested to correlate the persistent homology of a fixed time snapshot of the condensing droplets with future coalescence events. For that reason we replaced the Euclidean distance between the centers with the distance between drop borders when comparing with the filtration parameter values to define the complexes, in a sort of modified Vietoris-Rips complex (MVRC). The most evident effect of this paradigm change is that the β_0 and β_1 are shifted to lower filtration parameter values (Fig. 4).

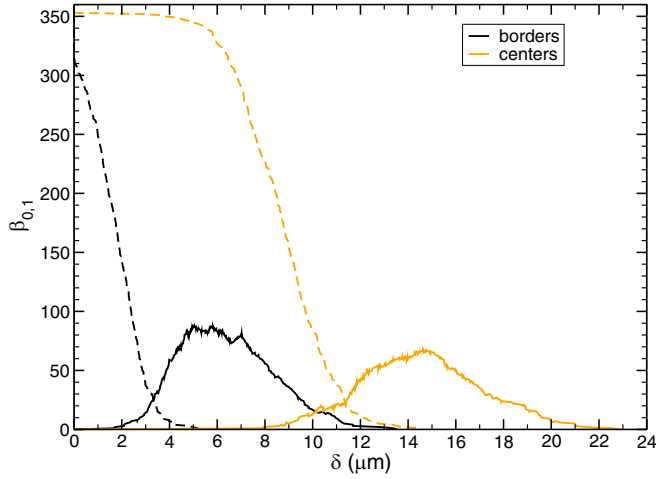


FIG. 4. Betti numbers for dimensions 0 (number of connected components; dashed lines) and 1 (number of loops, excluding triangles; solid lines) at $t = 180$ s, comparing the high case where the Vietoris-Rips complex is obtained through the centers of the droplets (light [orange] lines) or their borders (modified Vietoris-Rips complex; black lines) vs filtration parameter.

We verified that the MVRC filtration is stable under small perturbations for the bottleneck distance [26] (data not shown). Further details of the method used are explained in the following sections.

IV. RESULTS AND DISCUSSION

First, we check whether the assumption of having complete spatial randomness (CSR) in the nucleation sites is a good approximation in our experiments. CSR corresponds to a Poisson point process [27–29]. In Fig. 5 we plot the Ripley-Besag

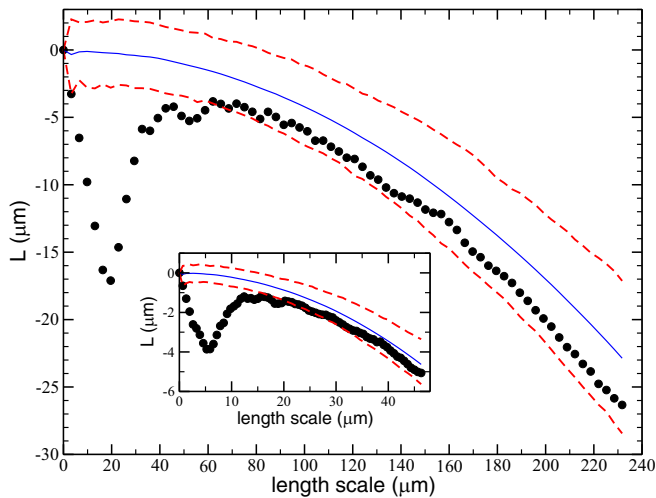


FIG. 5. L function for the measured droplets centers at the first time considered (180 s, circles) for the uncoated substrate. The solid line corresponds to a simulation of 10^3 realizations of a Poisson point process with the same number of points as in the experiment. The dashed lines are the boundaries of a 95% confidence interval for complete spatial randomness. The inset shows the same information, but for the high case.

L function for the uncoated substrate. We observe that at short-length scales, the distribution of the nucleation sites where droplets emerge is more dispersed than one completely random (solid line [simulated data] and dashed lines [estimated boundaries for the 95% confidence interval]). This is due to the coalescence of neighboring droplets at the beginning of the experiment that depletes the closest droplets. Preliminary measurements at earlier times show a better agreement. The Ripley-Besag functions for the coated substrates behave qualitatively like the uncoated (none case). For the purpose of comparison, a plot representing the high case is located in an inset enclosed within the figure. Consequently, we consider the distribution of nucleation sites as a homogeneous and isotropic point Poisson process. It's important to note that even in a perfect CSR finite structure, the L function is negative due to edge effects [30].

Stage 1 (nucleation) occurs at the beginning of the experiment ($t \ll 180$ s). Nucleation events happen in the static nucleation sites, where the energy barrier to nucleate is low. Thus, in this work, the change in the number of droplets only comes from coalescence events until new droplets emerge at much longer times (see the Supplemental Material [23]). In stages 2 and 3, the coalescence events do not dominate over the growth by condensation. However, they are not negligible (see below).

The active nucleation sites define an initial density (ρ_0) on a substrate of area S . In a circle of radius Δ , the mean number of nuclei is $\rho_0 \pi \Delta^2$. Thus, on average, a droplet of radius Δ has undergone $\rho_0 \pi \Delta^2 - 1$ coalescence events. For a given droplet, modeled as its projection circle to the substrate, an infinitesimal change in its area triggers coalescence events, and the local density decreases proportionally to $\rho_0 d(\pi \Delta^2)$. For the complete system, with density ρ ,

$$d\rho = -\rho \pi \rho_0 d(\Delta^2) \Rightarrow \frac{\rho}{\rho_0} = e^{-\rho_0 \pi \Delta^2}, \quad (1)$$

where the right-hand side of the last equation is the complementary cumulative distribution function of the distance from the center of a given randomly chosen droplet to its nearest neighbor for a complete spatial random process [30]. In other words, it is the probability that a drop has no neighbors at distances smaller than Δ or, from a physics perspective, that it has not coalesced.

The individual growth of drops under different conditions and assumptions usually leads to differential equations with solutions related to power laws. In general, a good approximation is: $r_i(t) = (r_{i0}^\alpha + Dt)^{\frac{1}{\alpha}}$ [3]. In our experimental conditions, the system can be approached as being equivalent to the growth of a film [3,11] leading to a value $\alpha = 3$. We measured the growth of individual droplets. In the none case, we took 14 among the most long-lived (i.e., without coalescence), and we obtained a value $\alpha = 2.9 \pm 0.3$. For the other cases, the high initial density makes coalescence events more frequent and the interaction between droplets higher. The evolution of the least interacting droplets is compatible with this value of α .

We consider that all droplets nucleate at time $t = 0$ from very small clusters of water molecules (the critical radius of nucleation for our experimental conditions is ~ 3 nm; see the Supplemental Material [23]). At the first time of observation

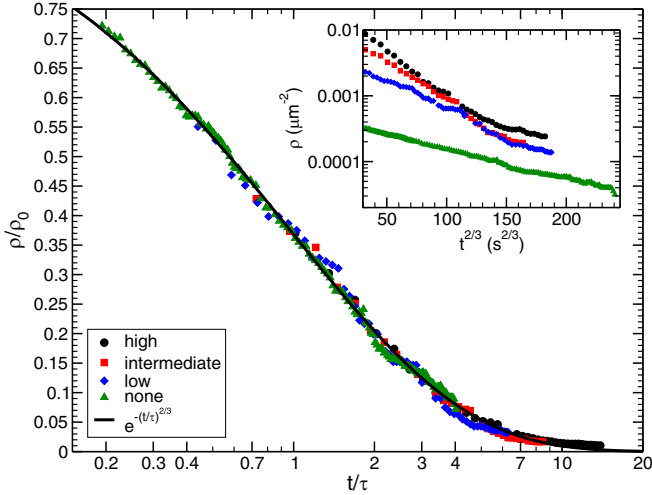


FIG. 6. Dimensionless density of droplets as a function of dimensionless time, for the four studied cases. Although the substrates are quite different, their densities follow a single stretched exponential curve. The inset shows the raw data.

(180 s), coalescence events are relatively few, and consequently, all nucleated droplets have a very similar size whose radii can be approximated by $(Dt)^{1/\alpha}$.

Then, a coalescence event between two droplets occurs when the distance between them becomes $2(Dt)^{1/\alpha}$, where D (see Sec. 6.1.2 of [3]) is proportional to $(\gamma\rho_0)^{-1}$ [at least when $\alpha = 3$, then $D \equiv C(\gamma\rho_0)^{-1}$], where γ is the volume coefficient of a droplet which for a spherical cap-shaped one depends only on the contact angle θ . Thus, $\gamma_i \equiv V_i/r_i^3$ (i subindex refers to an individual droplet's volume and measured radius, respectively). For short times, when coalescence events are not dominant, γ is the same for all BF droplets. However, it depends on the substrate.

If we plug it into Eq. (1), we obtain

$$\rho/\rho_0 = e^{-\rho_0\pi 4(Dt)^{2/\alpha}} = e^{-\rho_0^{1-2/\alpha}\pi 4(Ct/\gamma)^{2/\alpha}}, \quad (2)$$

which is a stretched exponential in t , for $\alpha > 2$.

Equation (2) can be expressed as

$$\rho/\rho_0 = e^{-(t/\tau)^{2/\alpha}}, \quad (3)$$

where $\tau = \gamma(4\pi)^{-\alpha/2}C^{-1}\rho_0^{1-\alpha/2}$.

At short times, Eq. (3) is a good approximation for droplets whose centers are distributed by a homogeneous isotropic point Poisson process (CSR). For the rest of the article, we will consider $\alpha = 3$.

In the inset of Fig. 6, we plot the density ρ as a function of time. We fit the data, at short times, with the stretched exponential function $\rho = \rho_0 e^{-(t/\tau)^{2/3}}$, which allows us to find for each condition a characteristic time τ and an initial density ρ_0 . The main figure shows the values of the inset, rescaled with ρ_0 and τ leading to a good collapse of all data to a single curve, even at longer times.

τ/γ fits with a power law vs ρ_0 ,

$$\tau/\gamma = 6\rho_0^{-0.55}, \quad (4)$$

with a 95% confidence interval for the exponent $(-0.68, -0.42)$ and for the coefficient (5, 7). The expected

exponent if $\alpha = 3$ is $-1/2$. Here we observe a decrease in the characteristic time as initial density increases, due to the enhanced coalescence between closer droplets (see the Supplemental Material [23] for more details). The initial density is consistent with the apparent number of nucleation sites.

Beysens and Knobler [31] stated that the condensed volume depends on the humid air flux and the difference in the partial water vapor pressure of the air and the saturation pressure at the substrate temperature. In general, the characteristic time [Eq. (4)] depends on the air flux and pressure differences (through the coefficient of the equation) and on the density. Since all our experiments had the same values of air flux (von Neumann boundary conditions) and saturation, the total condensed volume per unit area, h , in the stationary state should increase at the same constant rate for all the substrates. Accordingly, the fewer the number of accessible sites, the greater the amount of moisture available to be absorbed by every single droplet.

The condensed volume per unit area h can also be obtained as follows:

$$h \equiv \frac{\sum_{i=1}^N V_i}{S} = \frac{\gamma \sum_{i=1}^N r_i^3}{S} = \frac{\gamma N \langle r^3 \rangle}{S} = \gamma \rho \langle r^3 \rangle, \quad (5)$$

where S is the substrate's area of observation, the index i refers to the individual droplets, r_i is the apparent (i.e. measured) radius of droplet i , and γ is an r^3 -weighted average of the volume coefficient γ_i .

Since the conditions in the condensation chamber are stationary for all the considered times ($t \geq 180$ s), then $h \sim t$. If we write Eq. (5) in dimensionless form, γ cancels out, and $\langle r^3 \rangle \rho_0^{3/2} \sim t^+ e^{(t^+)^{2/3}}$, where $t^+ \equiv t/\tau$ is the dimensionless time. Our experimental results follow this behavior. In Fig. 7 the average radii of droplets are plotted against the dimensionless time. There we can observe two distinguished regimes: for short times, the curves seem to follow a power law with exponent 0.5, while at longer times the curves follow a proportionality trend. All the curves collapse into a single one, except for very late dimensionless times, where new droplets nucleate and grow. Thus, we conclude that our characteristic densities ρ_0 and times τ are well chosen.

The fit in the figure assumes that the trend of $\langle r^3 \rangle$ with time is the same as $\langle r \rangle^3$. This happens if and only if the radius density distribution scales with $\langle r \rangle$, and its time dependence is only through $\langle r \rangle$. The assumption is only approximate and further research is encouraged. Then we fit the data with $\langle r \rangle \rho_0^{1/2} = A(t^+ e^{(t^+)^{2/3}})^{1/3}$, where $A = 0.41$ is the fitting constant. We do not consider points related to new nucleations at long times ($t > 9\tau$). The power law with exponent $\mu_0 = 1/3$ [2,11,12,31] at short times is not observed, because the studied period starts in the crossover from $\mu_0 = 1/3$ to the next stage. If we extend the fit to even shorter times, the model predicts the $1/3$ exponent asymptotic behavior. For longer times, a power law with exponent $\mu = 3\mu_0$ was expected [2,12,31].

We see that, despite that the model is justified only at short times, it happens to fit well over the whole range of data, only starting to fail when the appearance of new nucleations is apparent (stage 5).

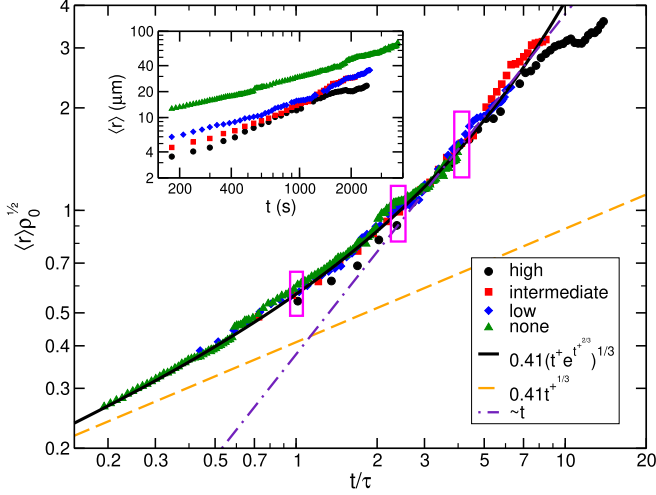


FIG. 7. Dimensionless average radius vs dimensionless time t^+ for the used substrates. All cases collapse on a single curve except for long dimensionless times, where new droplets have emerged. The dashed-dotted line is proportional to t , and the curved (black) solid line is a fit to a stretched exponential related function (see text and legend). The (orange) dashed line is its approximation for $t^+ \ll 1$. The experimental points approach asymptotically this power law. The boxes define dimensionless times where topological properties will be compared among the different cases. Inset: Original dimensional average radii.

The surface number density indicates the population of the droplet distribution, but to know how much of the surface is being used in condensation we analyze the surface coverage, ε^2 :

$$\varepsilon^2 \equiv \frac{\sum_{i=1}^N \pi r_i^2}{S} = \frac{\pi N \langle r^2 \rangle}{S} = \pi \rho \langle r^2 \rangle. \quad (6)$$

The coefficient of variation ($\sigma_r / \langle r \rangle$) for each case is almost constant along time (except for long times in the high-density case, when new nucleations take place). In the high-density case (excluding long-times data, $t > 9\tau$), it is 0.37 ± 0.04 , while in the intermediate case 0.22 ± 0.02 , in the low case 0.22 ± 0.04 , and in the none case 0.23 ± 0.04 . The fact that the coefficient of variation is approximately constant justifies that we use the same functional form as the basis of the fits to all the moments. For further details, refer to the Supplemental Material [23].

The surface coverage is plotted in Fig. 8 as a function of dimensionless time. The solid line comes from Eq. (6) assuming that $\sqrt{\langle r^2 \rangle}$ follows the fit obtained in Fig. 7.

The horizontal lines in Fig. 8 correspond to the predicted saturation values [2]:

$$\varepsilon_\infty^2 = \begin{cases} 1 - \frac{\theta_m}{200} & \text{if } \theta_m \geq 90^\circ \\ 0.55 \sin^2 \theta_m & \text{if } \theta_m < 90^\circ \end{cases}; \quad (7)$$

in this case, the average contact angle θ_m is used, because when the saturation values may be reached, the number of coalescence events are frequent and the contact line recedes and advances in different positions of the same droplet.

It can be observed that the surface coverage increases to a maximum value, and then eventually decreases before

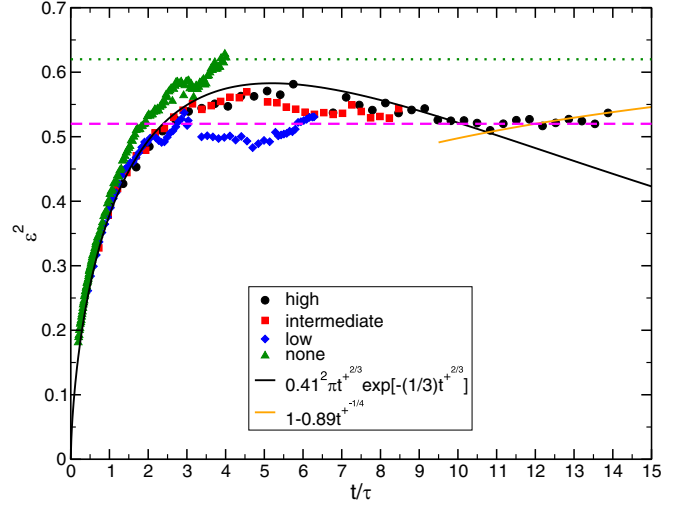


FIG. 8. Surface coverage of the droplets vs dimensionless time. The dotted line corresponds to the expected saturation values for the case none and the dashed line for the other cases (see text). The dark (black) solid line shows the expected values using the average radius and the surface number density fits. This holds fairly well before new droplets appear (stage 5) where the porosity ($1 - \varepsilon^2$) is expected to follow a power law with a $-1/4$ exponent [16]. The lighter (orange) solid line is a fit of those points to such expected law.

reaching stage 5, where the description based on quenched disorder is no longer valid. In the fully developed stage 5, which has not been completely reached in our data, the porosity $p \equiv 1 - \varepsilon^2$, is expected to follow a power law with an exponent of $-1/4$ [16]. Figure 8 shows that the experimental data points are compatible with this power law, as well as with the saturation values mentioned earlier.

Next, for each snapshot, we build a filtration with the distance between droplets, to obtain the corresponding Betti numbers. Space and time are made dimensionless with the same characteristic distances and times as above ($\rho_0^{-1/2}$ and τ).

We use tools from PH to determine whether there are topological differences beyond the effect of density on the BF dynamics. In Fig. 9 we show the normalized Betti numbers β_0^* and β_1^* at a dimensionless time of 1.01 ± 0.02 , which corresponds to a region where coalescence events are not predominant (first box in Fig. 7). The normalization for β_0 is performed with the number of droplets, and for β_1 with the number of squares (i.e., cycles other than triangles) in a perfectly square lattice with the given number of droplets [22]. In the figure, we can observe that all initial cases (densities) give similar values of β_0^* and β_1^* , which means that, statistically, the homology and the disorder structure are similar. The maximum value of the proportion of holes lies between 0.2 and 0.3 and is approximately the same for all cases, as well as the proportion of connected components.

It is possible to overlay the VRC onto the BF image. Figure 10 shows the corresponding VRC for dimensionless filtration parameters in the range of 0.78 ± 0.08 (where 0.08 is the standard deviation of the four parameters, which correspond specifically to the maxima of the Betti 1 number in

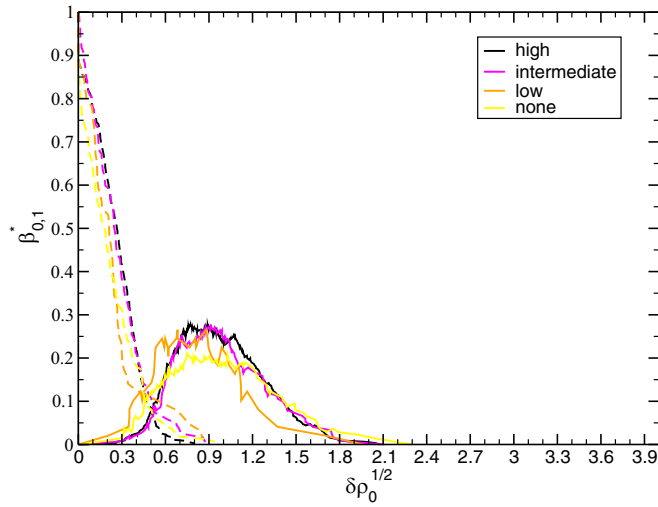


FIG. 9. Normalized Betti number for dimension 0 (dashed lines) and 1 (solid lines) vs filtration parameter at dimensionless time 1.01. From darkest to lightest (black, magenta, orange, yellow): high, intermediate, low, and none experiments.

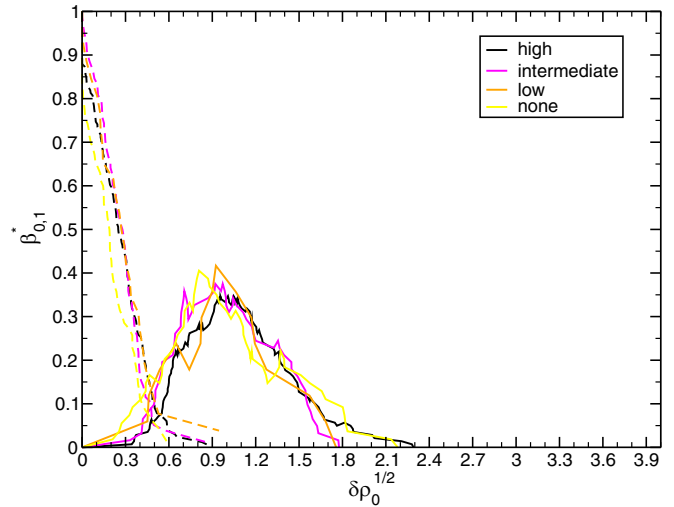


FIG. 11. Normalized Betti number for dimension 0 (dashed lines) and 1 (solid lines) vs filtration parameter at dimensionless time 2.40. From darkest to lightest (black, magenta, orange, yellow): high, intermediate, low, and none experiments.

each case). It should be noted that Fig. 10(a) has a different horizontal field of view (HFOV).

In Fig. 11 we compare the normalized Betti numbers of the different cases at dimensionless time 2.40 ± 0.02 (a region where coalescence events are more frequent; second box in Fig. 7); we observe that they are similar among them too. Compared to Fig. 9, the maximum value of the proportion of holes (β_1^*) increases (up to 0.4) and their peaks become sharper.

At later dimensionless times (e.g., Fig. 12, corresponding to 4.07 ± 0.04 ; third box in Fig. 7), the Betti numbers for the different cases differ more. This could be because the statistics

is poorer. Clearly the β_1^* curves are wider and displaced to higher dimensionless filtration parameters, when compared to earlier times (Figs. 9 and 11).

In the BF context a coalescence event occurs at a given time when the distance between the centers of two droplets (d_{ij}) becomes smaller than the sum of their radii. This point corresponds to a value of the filtration parameter $\delta = 0$ in the MVRC and to $\Delta = d_{ij}$ in a standard Vietoris-Rips complex. If we consider all the droplets on the surface, it is possible to relate both of these values to a quantity that is linked to the distribution of radii in the BFs. This quantity, when made dimensionless, should be the same regardless of the original distribution of droplets if there is complete spatial randomness. Therefore, it is convenient to consider (in dimensionless

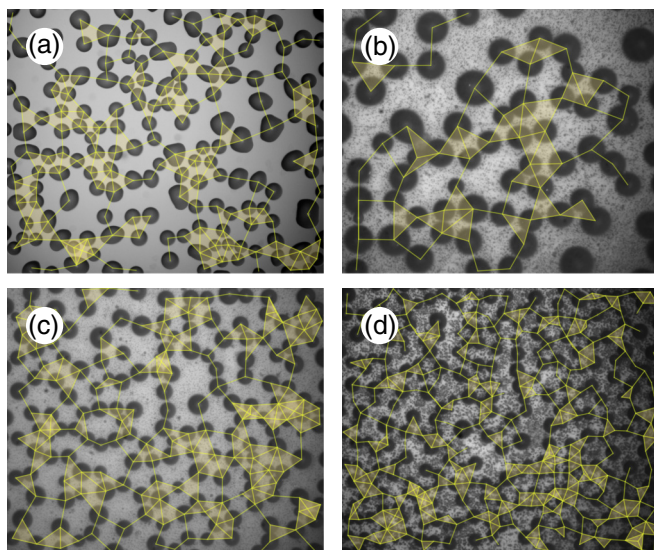


FIG. 10. Vietoris-Rips complexes at dimensionless time 1.01 and dimensionless filtration parameter 0.78 ± 0.08 . (a) None, (b) low, (c) intermediate, and (d) high, where HFOV is (a) 1.104 mm and [(b)–(d)] 0.220 mm.

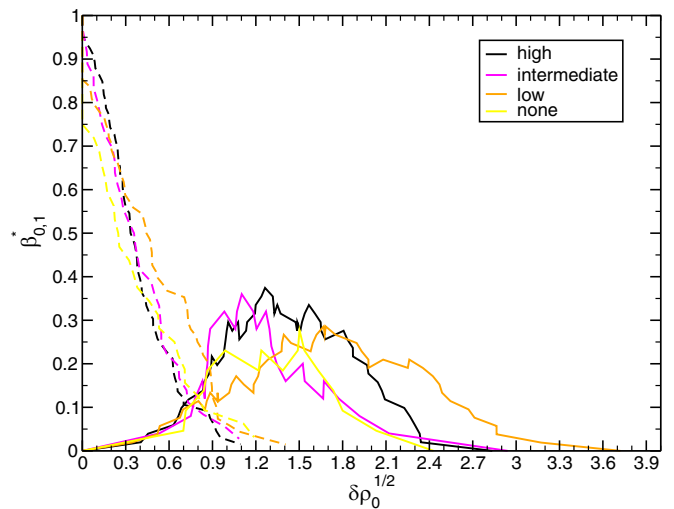


FIG. 12. Normalized Betti number for dimension 0 (dashed lines) and 1 (solid lines) vs filtration parameter at dimensionless time 4.07. From darkest to lightest (black, magenta, orange, yellow): high, intermediate, low, and none experiments.

variables):

$$\Delta^+ \equiv \delta^+ + x\langle r^+ \rangle, \quad (8)$$

where x is an unknown function of t^+ with expected values of the order of 1, and $\langle r^+ \rangle$ is the average radius (extracted from Fig. 7).

We obtain β_0^* for all the cases and dimensionless times (data not shown). We aim to fit all β_0^* curves with Gaussian functions displaced by $x\langle r^+ \rangle$ to get a smooth estimation of their spread (i.e., standard deviation):

$$\beta_0^* = \exp \left[-\frac{(x\langle r^+ \rangle + \delta^+)^2 - x^2\langle r^+ \rangle^2}{2\sigma_{\beta_0^*}^2 \rho_0} \right]. \quad (9)$$

The slope of β_0^* at the origin is inversely proportional to its variance and proportional to x :

$$\left. \frac{\partial \beta_0^*(\delta^+; t^+)}{\partial \delta^+} \right|_{\delta^+=0} = -\frac{x\langle r^+ \rangle}{\sigma_{\beta_0^*}^2 \rho_0}. \quad (10)$$

In this equation we can see that β_0 (or β_0^*) can be expressed in our system as a function of two variables (δ and t , or their dimensionless variations).

If the number of connected components is constant, then by the implicit function theorem:

$$\frac{d\delta}{dt} = -\frac{\partial \beta_0}{\partial t} \left(\frac{\partial \beta_0}{\partial \delta} \right)^{-1}. \quad (11)$$

Evaluating Eq. (11) in $\delta = 0$ and $t = t_0$ and using that $\beta_0(\delta = 0, t = t_0) = N(t_0)$, where $N(t_0)$ is the number of BF droplets at time t_0 . Then

$$\left. \frac{d\delta}{dt} \right|_{t=t_0} = -\left. \frac{dN}{dt} \right|_{t=t_0} \left(\left. \frac{\partial \beta_0}{\partial \delta} \right|_{\delta=0} \right)^{-1}.$$

Note that the last equation relates the (spatial) topology at a given time with the evolution of the coalescence events in the future. If now we put the left-hand side of the equation as a function of $\langle r \rangle$ (by using the chain rule):

$$\left. \frac{d\delta}{d\langle r \rangle} \right|_{\langle r \rangle = \langle r \rangle(t_0)} = -\left. \frac{dN}{dt} \right|_{t=t_0} \left(\left. \frac{\partial \beta_0}{\partial \delta} \right|_{\delta=0} \frac{d\langle r \rangle}{dt} \right|_{t=t_0} \right)^{-1}.$$

After that, we make all quantities dimensionless and properly scaled (e.g., $\beta_0 = N\beta_0^*$), and remove the evaluation points when they are obvious. That gives

$$\frac{d\delta^+}{d\langle r^+ \rangle} = -\frac{1}{\rho^+} \frac{d\rho^+}{dt^+} \left(\left. \frac{\partial \beta_0^*}{\partial \delta^+} \right|_{\delta^+=0} \frac{d\langle r^+ \rangle}{dt^+} \right)^{-1}. \quad (12)$$

Using Eq. (8), and taking Δ^+ constant, we obtain

$$\frac{d\delta^+}{d\langle r^+ \rangle} = -x, \quad (13)$$

and if we plug Eqs. (13) and (10) into Eq. (12), then

$$\frac{x^2}{\sigma_{\beta_0^*}^2 \rho_0} = -\frac{1}{\rho^+} \frac{d\rho^+}{dt^+} \left(\langle r^+ \rangle \frac{d\langle r^+ \rangle}{dt^+} \right)^{-1}. \quad (14)$$

Note that the right-hand side of Eq. (14) is a function of t^+ and that both experimental data values and the fits to the scaling model can be used to determine a value for each t^+ .

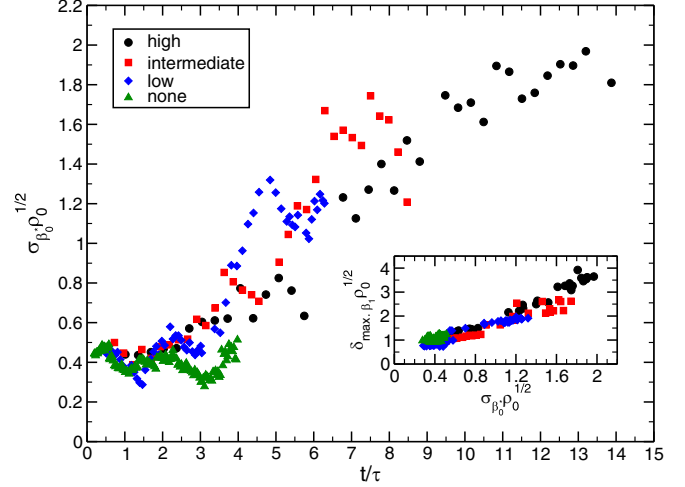


FIG. 13. Characteristic dimensionless width of Betti number for dimension 0 vs dimensionless time. It was obtained as the standard deviations of the Gaussian functions that fit the data self-consistently (see text). In the inset the dimensionless filtration parameter for which β_1 is maximum is plotted against the dimensionless width of β_0^* .

Finally, we fit Eq. (9) to all β_0^* curves, self-consistently with Eq. (14).

In Fig. 13 the dimensionless width of β_0^* (the standard deviation of the Gaussian fit, $\sigma_{\beta_0^*} \rho_0^{1/2}$, calculated as stated above) is shown as a function of dimensionless time. At low times ($t^+ < 2$), where the growth of droplets is mostly homogeneous due to diffusion with relatively few coalescence events, the positions of the droplets do not change much. Therefore, the starting point to measure distances in the MVRC moves according to the droplet radii. Consequently, the nodes (droplets) link at similar filtration parameters, leading to a narrow β_0^* (number of connected components). In fact, in the region where Eq. (1) holds asymptotically, the aforementioned standard deviation is nearly constant.

When coalescence events dominate the growth ($t^+ \gtrsim 2$), the distances between coalescing droplets and others increase with a linear trend, resulting in a wider β_0 as dimensionless time increases.

We also obtain all β_1^* curves (data not shown). We fit them with Gaussian functions to get a smooth estimation of their displacement with respect to the origin, their maximum value, and their spread (i.e., standard deviation). As the structure of droplets is not a perfect triangular lattice, when around one link per droplet is formed, the complex starts to have holes and β_1^* becomes bigger than 0. Consequently, the position of the maximum of the β_1^* curve behaves similarly to the width of β_0^* . In the inset of Fig. 13, the dimensionless filtration parameter for which β_1 is maximum according to a Gaussian fit is plotted against the dimensionless width of β_0^* .

In Fig. 14 the plot shows the derivative of the dimensionless filtration parameter δ^+ with respect to the average radius $\langle r^+ \rangle$ as a function of dimensionless time. When droplets are very small (i.e., at very short times $t^+ \ll 1$), almost all droplets have the same size. Therefore, they grow at the same rate, and an increase in $\langle r^+ \rangle$ is equivalent to a decrease of δ^+

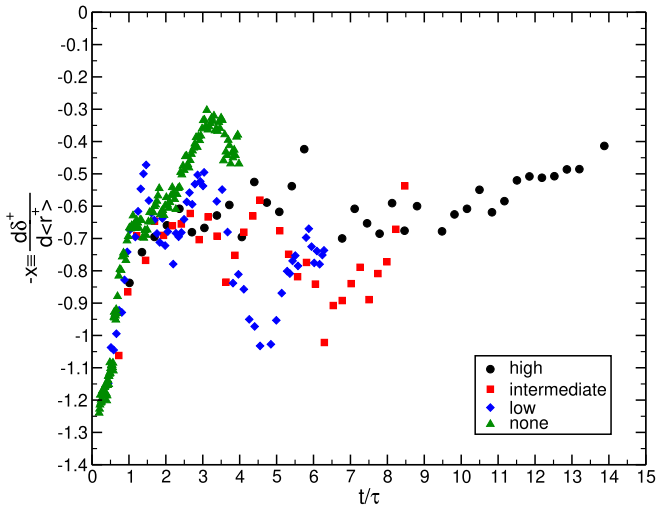


FIG. 14. Ratio between the infinitesimal change of the dimensionless filtration parameter δ^+ that is needed to balance an infinitesimal increase of the average radius $\langle r^+ \rangle$ to keep a constant characteristic width of β_0^* , as a function of dimensionless time.

twice the variation of radii. It is expected that x [in Eq. (13)] approaches 2 when $t^+ \rightarrow 0^+$. As time increases, but still coalescence events are not predominant, x rapidly decreases. This decrease indicates that there are more neighbors made of large drops or mixed ones than neighbors made up small droplets, as large droplets are randomly distributed on the surface. When coalescence events become more relevant ($t^+ \gtrsim 2$), there are high fluctuations around a value of $x \sim 0.7$. At later times, when new droplets appear, there is a slight decrease in x .

In Fig. 15 the maximum value of β_1^* according to the Gaussian fit is plotted against dimensionless time. It is possible to observe that the Betti numbers increase abruptly as time increases until a value of t/τ between 1 and 3 is reached. After that, the maxima decrease with a much smaller slope. Therefore, we can conclude that the complete spatial randomness existing in the nucleation sites leads to a small proportion

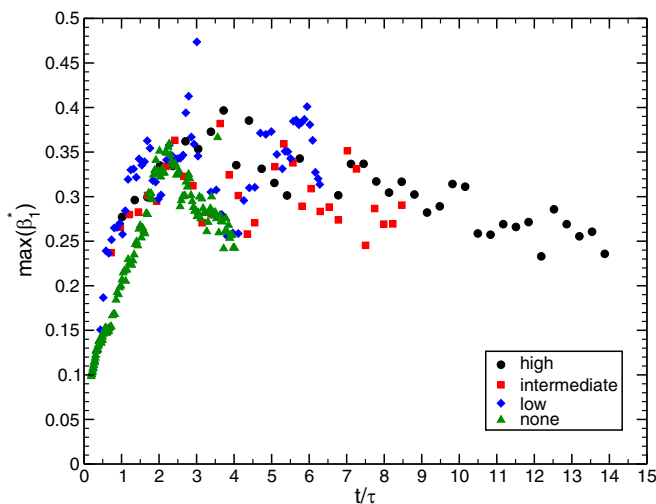


FIG. 15. Normalized maximum Betti number for dimension 1 vs dimensionless time.

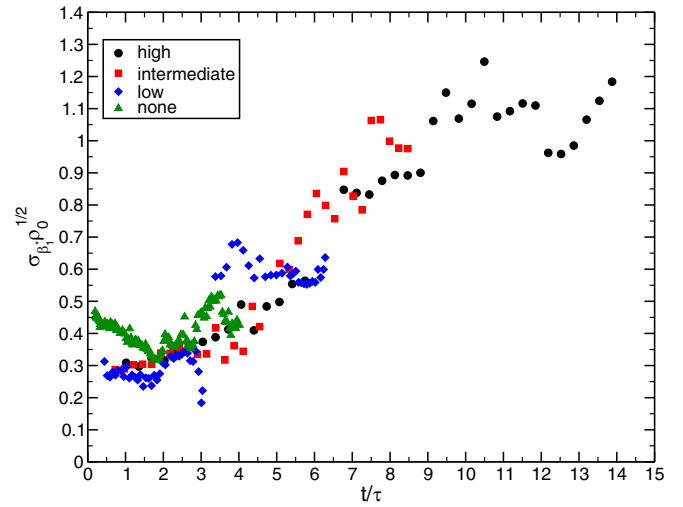


FIG. 16. Typical width of the region in the filtration parameter, where Betti number for dimension 1 is relevant vs dimensionless time. It was obtained as the standard deviation of the Gaussian functions that fit the data.

of holes in the corresponding complex, which increases with subsequent coalescence events. When coalescence events are dominant compared to diffusion in the growth of droplets, the proportion of holes decreases and asymptotically reaches a value of around 0.2–0.3, which corresponds to a self-similar structure [16].

These self-similarity effects can also be observed in Fig. 16, where the dimensionless width of β_1^* (standard deviation of the Gaussian fit) is shown as a function of the dimensionless time. The curves follow a similar trend as the dimensionless width of β_0^* (Fig. 13). When new droplets appear (in the self-similar stage), the observed width seems to have become stationary and fluctuating around a dimensionless value of 1, which defines, together with $\delta_{\max. \beta_1}$ (see inset of Fig. 13), the spatial range where holes are relevant.

V. CONCLUDING REMARKS

In conclusion, the spatial distribution of emerging droplets determines the evolution of the condensation pattern, irrespective of the details of the interaction between droplets. With very few assumptions, we derive a model of breath figure (BF) evolution for short times that performs well over a long range (up to stage 5) due to the nature of the complete spatial randomness (CSR) distribution of nucleation seeds and the fact that nucleation sites are fixed and do not relax thermodynamically (quenched disorder). We assume that droplets grow from very small nuclei that appear in a short time at the beginning of the experiment. If this were not the case, a more complex approach should be taken [32,33], even in the scenario where the centers of the nuclei exhibit a CSR distribution.

Once new droplets appear (stage 5), the distribution is no longer static, and nucleation events appear to be like sampling with replacement from the distribution of nuclei, compared to the case in which Eq. (1) holds. This stage may correspond to self-similar dynamics, and the approach given in this article must include new concepts [16]. This deviation is mostly

related to the structural differences between complete spatial randomness [30] and the self-similar stage. We encourage further study of that regime (long times) from a holistic point of view and also to confirm experimentally the validity of the model for much shorter times, where $t^{1/3}$ behavior could be observed.

Actually, the appearance of new droplets allows a slight increase in surface coverage at long dimensionless times ($t^+ \gg 1$), which would otherwise decrease. This has significant implications for applications such as water recovery, which indicate that coated substrates are a significant improvement. These substrates exhibit macroscopic hydrophobic behavior (see contact angles in Table 1 of the Supplemental Material [23]) with a high number density of hydrophilic nucleation sites where droplet nucleation events occur. The former favors shedding when the substrates are inclined, while the latter decreases the characteristic times (see the Supplemental Material [23]) of the growth dynamics. It is worth noting that the asymptotic value of surface coverage decreases as the macroscopic contact angle increases [2]. In applications, it is preferred to have small contact line pinning, resulting in increased shedding. Generally, contact angles higher than 90° are preferable.

These types of substrates are easier to fabricate compared to tailored regular lattices, which may also have interesting properties (e.g., even higher contact angles and a high number density of nucleation sites). However, it is important to keep in mind that the use of BFs in real-world applications has very different boundary conditions [2]. Having a humidity reservoir (Dirichlet boundary condition) is more desirable than a constant humidity flux (von Neumann boundary condition) used here, which in turn makes the recovered water rate constant at the stationary state. With our conditions, the recovered water does not depend on the substrate.

We also compared the condensation patterns that appear on substrates with different densities of nucleation sites using classical techniques and persistent homology. Both approaches give consistent results and are similar among the different densities of sites when the dimensionless magnitudes are considered. To obtain the dimensionless magnitudes, we used the typical time and characteristic initial surface number density obtained from stretched exponential fits coming from

the scaling model [Eq. (3)]. With those fits, we achieved very good (to fair, depending on the magnitudes) collapse to single curves of all the data. Thus, by varying the number of nucleation sites but keeping the other experimental conditions the same, the scaled behavior is equivalent for both macroscopic averages and topological features.

We were able to establish a connection between the BF topological properties at a particular time and the coalescence events that would occur at later times. At short times, there is a clear collapse of the data (Fig. 14) that demonstrates this relationship. However, at long times, the collapse is less evident, and further research is required, perhaps using other more informative quantities of persistent homology, such as the barcodes in different dimensions. If a universal behavior for $\frac{d\delta^+}{d(r^+)}$ at all times could be determined, it would be possible to predict future coalescence events statistically. Otherwise, predictions could be made only locally, and the calculation of persistent homology would have to be performed for all times.

Finally, we have demonstrated that global boundary conditions (number density of nucleation sites, air flow rate, etc.) have a greater influence on the statistics and topology of BF evolution than individual growth models.

ACKNOWLEDGMENTS

This work was partly supported by the Spanish MCIN/EI/10.13039/501100011033 (Grants No. FIS2017-83401-P and No. PID2021-129066NA-I00) and by “ERDF A Way of Making Europe.” R.U. acknowledges financial support from the “Asociación de Amigos de la Universidad de Navarra.” We thank the developers of the “poinpats” (PySAL) Python library for the analysis of point patterns randomness [34], the developers of the “persim” and “ripser” Python libraries for the analysis of persistent homology [35], and Luis Fernando Urrea for technical support. We also thank Sergio Ardanza-Trevijano for fruitful discussions, M. A. Miranda for critical reading of the manuscript, and the anonymous reviewers for fruitful suggestions.

R.U. conducted the experiments, and W.G. conceived the original idea and derived the model. Both authors contributed equally to the other research tasks and manuscript preparation.

-
- [1] S. F. Edwards and P. W. Anderson, Theory of spin glasses, *J. Phys. F* **5**, 965 (1975); M. Mézard, G. Parisi, and M. A. Virasoro, *Spin Glass Theory and Beyond: An Introduction to the Replica Method and Its Applications* (World Scientific, Singapore, 1987), Vol. 9.
 - [2] See D. Beysens, *Dew Water*, River Publishers Series in Chemical and Environmental Engineering (River Publishers, Gistrup, Denmark, 2018) and references therein.
 - [3] D. Beysens, *The Physics of Dew, Breath Figures and Dropwise Condensation*, Lecture Notes in Physics Vol. 994 (Springer, 2022).
 - [4] M.-G. Medici, A. Mongruel, L. Royon, and D. Beysens, Edge effects on water droplet condensation, *Phys. Rev. E* **90**, 062403 (2014).
 - [5] C. Schäfle, P. Leiderer, and C. Bechinger, Subpattern formation during condensation processes on structured substrates, *Europhys. Lett.* **63**, 394 (2003).
 - [6] S. Nath, S. F. Ahmadi, and J. B. Boreyko, A review of condensation frosting, *Nanoscale Microscale Thermophys. Eng.* **21**, 81 (2017).
 - [7] J. B. Boreyko, R. R. Hansen, K. R. Murphy, S. Nath, S. T. Retterer, and C. P. Collier, Controlling condensation and frost growth with chemical micropatterns, *Sci. Rep.* **6**, 19131 (2016).
 - [8] P.-B. Bintein, H. Lhuissier, A. Mongruel, L. Royon, and D. Beysens, Grooves accelerate dew shedding, *Phys. Rev. Lett.* **122**, 098005 (2019).
 - [9] J. Trosseille, A. Mongruel, L. Royon, M.-G. Medici, and D. Beysens, Roughness-enhanced collection

- of condensed droplets, *Eur. Phys. J. E* **42**, 144 (2019).
- [10] H. Zhao and D. Beysens, From droplet growth to film growth on a heterogeneous surface: Condensation associated with a wettability gradient, *Langmuir* **11**, 627 (1995).
- [11] M. Sokuler, G. Auernhammer, C. Liu, E. Bonaccorso, and H.-J. Butt, Dynamics of condensation and evaporation: Effect of inter-drop spacing, *Europhys. Lett.* **89**, 36004 (2010).
- [12] D. Beysens, Dew nucleation and growth, *C. R. Phys.* **7**, 1082 (2006).
- [13] P. Meakin, Droplet deposition growth and coalescence, *Rep. Prog. Phys.* **55**, 157 (1992).
- [14] J. A. Blackman and S. Brochard, Polydispersity exponent in homogeneous droplet growth, *Phys. Rev. Lett.* **84**, 4409 (2000).
- [15] J. Blaschke, T. Lapp, B. Hof, and J. Vollmer, Breath figures: Nucleation, growth, coalescence, and the size distribution of droplets, *Phys. Rev. Lett.* **109**, 068701 (2012).
- [16] L. Stricker, F. Grillo, E. A. Marquez, G. Panzarasa, K. Smith-Mannschott, and J. Vollmer, Universality of breath figures on two-dimensional surfaces: An experimental study, *Phys. Rev. Res.* **4**, L012019 (2022).
- [17] D. Fritter, C. M. Knobler, and D. A. Beysens, Experiments and simulation of the growth of droplets on a surface (breath figures), *Phys. Rev. A* **43**, 2858 (1991).
- [18] F. Family and P. Meakin, Kinetics of droplet growth processes: Simulations, theory and experiments, *Phys. Rev. A* **40**, 3836 (1989).
- [19] R. Seco-Gudiña, J. Guadarrama-Cetina, and W. González-Viñas, Dynamics of water condensation over arrays of hydrophilic patches, *Eur. Phys. J. Special Topics* **226**, 1189 (2017).
- [20] H. Edelsbrunner and J. Harer, *Computational Topology: An Introduction* (American Mathematical Society, Providence RI, USA, 2010).
- [21] S. Ardanza-Trevijano, I. Zuriguel, R. Arévalo, and D. Maza, Topological analysis of tapped granular media using persistent homology, *Phys. Rev. E* **89**, 052212 (2014).
- [22] R. Aslam, S. Ardanza-Trevijano, K. M. Poduska, A. Yethiraj, and W. González-Viñas, Quantifying disorder in colloidal films spin-coated onto patterned substrates, *Phys. Rev. E* **95**, 032607 (2017).
- [23] See Supplemental Material at <http://link.aps.org/supplemental/10.1103/PhysRevE.108.065107> for further information on experimental details, nucleation and coalescence events in droplets, involved time-scales and the size distribution of droplets in the BF.
- [24] R. N. Leach, F. Stevens, S. C. Langford, and J. T. Dickinson, Dropwise condensation: Experiments and simulations of nucleation and growth of water drops in a cooling system, *Langmuir* **22**, 8864 (2006).
- [25] J. E. Castillo and J. A. Weibel, Predicting the growth of many droplets during vapor-diffusion-driven dropwise condensation experiments using the point sink superposition method, *Int. J. Heat Mass Transf.* **133**, 641 (2019), and references therein.
- [26] D. Cohen-Steiner, H. Edelsbrunner, and J. Harer, Stability of persistence diagrams, *Discrete Comput. Geom.* **37**, 103 (2007).
- [27] B. D. Ripley, Tests of ‘randomness’ for spatial point patterns, *J. R. Stat. Soc. B* **41**, 368 (1979).
- [28] G. Lang and E. Marcon, Testing randomness of spatial point patterns with the Ripley statistic, *ESAIM: Probab. Stat.* **17**, 767 (2013).
- [29] G. Arbia, G. Espa, D. Giuliani, and M. M. Dickson, Effects of missing data and locational errors on spatial concentration measures based on Ripley’s K -function, *Spatial Econ. Anal.* **12**, 326 (2017).
- [30] B. D. Ripley, *Spatial Statistics*, Wiley Series in Probability and Statistics (Wiley-Interscience, Hoboken NJ, USA, 2004).
- [31] D. Beysens and C. M. Knobler, Growth of breath figures, *Phys. Rev. Lett.* **57**, 1433 (1986).
- [32] S. Torquato, B. Lu, and J. Rubinstein, Nearest-neighbor distribution functions in many-body systems, *Phys. Rev. A* **41**, 2059 (1990); M. Tomellini, Interface evolution in phase transformations ruled by nucleation and growth, *Physica A* **558**, 124981 (2020).
- [33] M. Tomellini and M. Fanfoni, Connection between phantom and spatial correlation in the Kolmogorov-Johnson-Mehl-Avrami-model: A brief review, *Physica A* **590**, 126748 (2022).
- [34] S. J. Rey and L. Anselin, PySAL: A Python library of spatial analytical methods, *Rev. Region. Stud.* **37**, 5 (2007).
- [35] N. Saul and C. Tralie, Scikit-TDA: Topological data analysis for Python, <https://doi.org/10.5281/zenodo.2533369> (2019); C. Tralie, N. Saul, and R. Bar-On, Ripser.py: A lean persistent homology library for Python, *J. Open Source Softw.* **3**, 925 (2018).